CUSRA2021: A Radially Anisotropic Model of the Contiguous US and surrounding regions by full-waveform inversion

Tong Zhou[1], Jiaqi Li[2], Ziyi Xi[1], Guoliang Li[3], and Min Chen[1]

[1]Michigan State University
[2]University of California, Los Angeles
[3]University of Southern California

November 18, 2022

Abstract

The lithospheric structure of the contiguous US and surrounding regions is significant in revealing the historical tectonic deformations and interactions between subducting slabs and cratons. In this paper, we present a new radially anisotropic shear wave speed model of this region, constrained by seismic full-waveform inversion. The new model (named CUSRA2021) utilizes frequency dependent travel time measured from waveforms of 160 earthquake events recorded by 5,280 stations. More earthquakes located in contiguous US are incorporated to improve the data coverage in eastern US. The final model exhibits clear and detailed shear wave speed anomalies that correlate very well with tectonic units such as North America Craton (high-Vs), Cascadia subduction zones (high-Vs), Columbia Plateau (low-Vs), Basin and Range (low-Vs), etc. In particular, the detail of the North America Craton beneath Illinois is revealed, and the depth of high-Vs anomaly beneath the North America Craton correlates well with S-to-P receiver function and SH reflection studies. The radial anisotropy also shows a layering of Craton lithosphere.

CUSRA2021: A Radially Anisotropic Model of the Contiguous US and surrounding regions by full-waveform inversion

Tong Zhou[1,2], Jiaqi Li[1,2], Ziyi Xi[1,3], Guoliang Li[1,4], Min Chen[1,3]

[1]Computational Mathematics, Science and Engineering, Michigan State University
[2]Earth Planetary and Space Sciences, University of California, Los Angeles
[3]Earth and Environmental Sciences, Michigan State University
[4]Department of Earth Sciences, University of Southern California

Key Points:

- A new radially anisotropic shear wave speed model for the contiguous US using full waveform tomography is derived.
- Eastern US data coverage is enhanced by including intracontinental earthquakes and geographic station weighting.
- Radially anisotropic layering in the North America Craton region is widely observed and related to lithosphere accretion.

Corresponding author: Tong Zhou, `zhouton3@msu.edu,tzhou@epss.ucla.edu`

Abstract

The lithospheric structure of the contiguous US and surrounding regions is significant in revealing the historical tectonic deformations and interactions between subducting slabs and cratons. In this paper, we present a new radially anisotropic shear wave speed model of this region, constrained by seismic full-waveform inversion. The new model (named CUSRA2021) utilizes frequency dependent travel time measured from waveforms of 160 earthquake events recorded by 5,280 stations. More earthquakes located in contiguous US are incorporated to improve the data coverage in eastern US. The final model exhibits clear and detailed shear wave speed anomalies that correlate very well with tectonic units such as North America Craton (high-Vs), Cascadia subduction zones (high-Vs), Columbia Plateau (low-Vs), Basin and Range (low-Vs), etc. In particular, the detail of the North America Craton beneath Illinois is revealed, and the depth of high-Vs anomaly beneath the North America Craton correlates well with S-to-P receiver function and SH reflection studies. The radial anisotropy also shows a layering of Craton lithosphere.

Plain Language Summary

Ancient continents (cratons) are cold, bouyant and have a thick root (lithosphere) down to about 200 km beneath the Earth's surface. In the contiguous US and surrounding regions, ancient continents (central and eastern US) were preserved and altered at the margins (western US). To better understand the possible process of historical geological events, we apply an advanced seismic imaging technique utilizing full seismic waveform to obtain the detailed structure of the contiguous US and surrounding regions. Here we apply more earthquakes located inside the US to improve the data coverage and finally observed that the lithosphere of eastern US generally has two layers with different seismic wave speeds in vertical directions. This observation correlates with previous studies and may indicate the formation and accretion process of cratons.

1 Introduction

Contiguous US and surrounding regions have complex geological units and deformation history. Among which, North America Craton (Figure 1) forms the stable core of the contiguous US. Hotspots, i.e., Yellowstone, and subduction processes since Mesozoic, i.e., Farallon and Cascadia, shaped the contiguous US region. The deformation processes draw people's attention and are extensively studied from different disciplines including geological, seismological, geochemical and geodynamical studies. Seismic tomography is one of the most important methods to image the subsurface structure and constrain various of rock properties including wave speeds, anisotropy and attenuation. Over the years, various tomographic work in multiple scales is applied to this region (Fichtner et al., 2009; Tape et al., 2010; Lekić & Romanowicz, 2011; Yuan et al., 2014; Schmandt & Lin, 2014; Shen & Ritzwoller, 2016; Zhu et al., 2017; Zhu, Yang, & Li, 2020; Krischer et al., 2018) and provide images of the contiguous US. Such images are indicative for current tectonic status and helpful for studying the dynamic processes of tectonic evolution. As the high-quality broadband seismic data accumulates, full-waveform inversion, one of the state-of-the-art seismic tomographic methods for the high-resolution and accurate waveform modelling using a spectral-element wave equation solver (SEM, (Komatitsch & Tromp, 2002b, 2002a)), is enabled to be applied in the global or regional seismic wave speeds tomography studies. Southern California crustal structure is the earliest example for the application of full-waveform inversion (Tape et al., 2009, 2010; Chen & Tromp, 2007). Crustal and mantle structure of Australia (Fichtner et al., 2009), Europe (Zhu et al., 2013), East Asia (Chen, Niu, Liu, & Tromp, 2015; Tao et al., 2018) and globe (Bozdağ et al., 2016; Lei et al., 2020) has been investigated using full-waveform inversion. Focusing on the North America, (Yuan et al., 2014) applied normal mode full-waveform tomography and reveals the large-scale structure of the North America Craton. (Zhu et al., 2017; Zhu, Yang, & Li, 2020) derived radial and azimuthal anisotropic models of the region and discovers possible toroidal flow of the Cascadia subduction zone (Zhu, Li, et al., 2020). (Krischer et al., 2018) applied an automatic full-waveform inversion method on the North America and derived another high-resolution radially anisotropic model. An application of box tomography jointing both teleseismic earthquakes and local earthquakes are introduced by (Clouzet et al., 2018). These models well correlate with each other in large-scale features. Nevertheless, the crustal and uppermost model structure manifests discrepancies in terms of small-scale heterogeneities, which is partially because of the difference of data set, frequency range, and initial model used in each tomographic work. Here, we present a new radially anisotropic model constrained by full-waveform tomography with broadband seismic data from 160 local and regional earthquake events and 5,280 stations, in the period range of 15 to 120 seconds. The initial model is constructed with a global mantle model and a jointly inverted model with ambient noise cross-correlations and receiver functions to get the optimal initial data coverage and enables more local earthquake events. Also, the radially anisotropic feature is now extended from typical only the upper mantle to the entire crust and upper mantle, from the surface to 670 km. This new model manifests major tectonic features in the contiguous US with shear wave speed and radial anisotropy anomalies, including Cascadia Subduction zone, Yellowstone Hotspot, Wyoming Plateau, Colorado Plateau, and North America Craton. These features correlate well with previous studies and exhibit enhancements on smaller scale tectonic structures, especially in Wyoming and Central US. In this paper, we focus on the details of model construction, quality assessment and model presentation. A very general discussion of some indicative features is also provided.

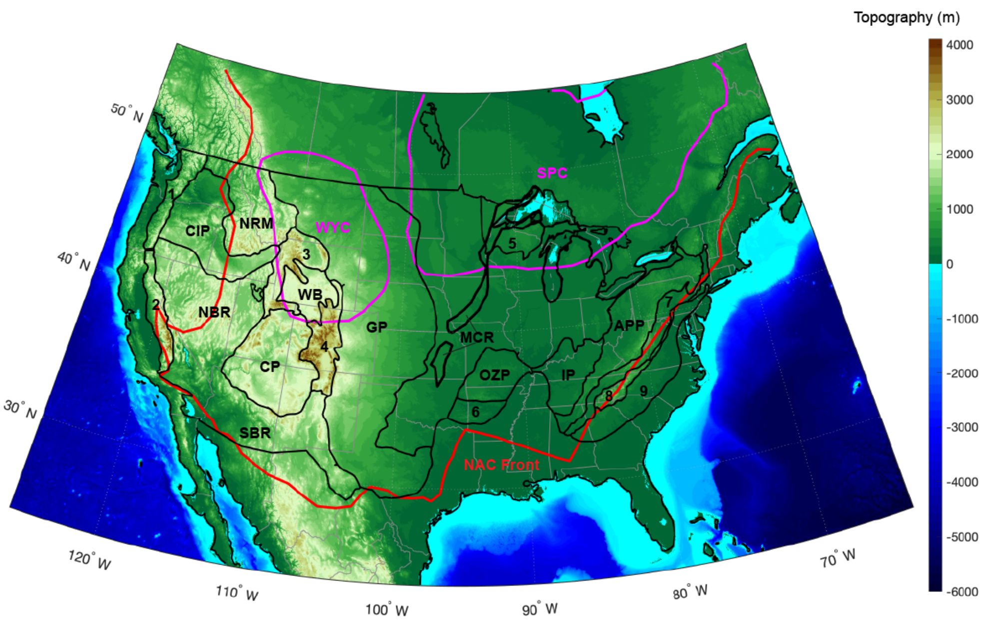

Figure 1. Contiguous US and its geophysical units, along with Craton boundaries. Black line marking the boundary of geophysical units. APP: Appalachian Mountain Plateaus; CIP: Columbia Igneous Plateau; CP: Colorado Plateaus; GP: Great Plains; IP: Interior Lowland Plateaus; NBR: North Basin and Range; OZP: Ozark Plateaus; SBR: South Basin and Range; WB: Wyoming Basin; 1: Cascade Mountains; 2: Sierra Mountains; 3: Middle Rocky Mountains; 4: Southern Rocky Mountains; 5: Superior Upland; 6: Ouachita; 7: Valley and Ridge; 8: Blue Ridge; 9: Piedmont. Boundary data is from United States Geological Survey and Fenneman and Johnson, 1948. Magenta line marks the Archean Cratons and rifting zones. WYC: Wyoming Craton; SPC: Superior Craton; MCR: Mid-Continental Rift. Red line marks the North America Craton Front. Craton boundaries are from (Yuan et al., 2014).

2 Data and Methods

2.1 Study region, earthquakes and stations

To utilize higher frequency waveforms while maintaining the computational cost reasonable, we have to select a relatively small region. Unlike previous studies including contiguous US region (Yuan et al., 2014; Zhu et al., 2017; Krischer et al., 2018), we exclude the Northern Atlantic ridge events but only focus on a region that covers North America Plate as well as part of the Caribbean Sea (Figure 2a). The computational domain is a $42° * 48°$ spherical trunk rotated 20° counterclockwise, and the region for inversion is excluding a 2° margin along the boundary and the depth range is from the Earth's surface down to 670 km. This study region utilizes the earthquake events in the western coast of the US, and the boundary of the Caribbean Sea plate.

We select 160 earthquake events within the study region to perform the inversion (Figure 2a). All available broadband seismic stations in the US, Canada, and Mexico (Detailed network contributions are listed in data acknowledgement) for a total of 5,280 are used. The events are mainly distributed in the Western US and Caribbean Sea plate. The selected events are within a time frame between 2005 and 2019 and have moment magnitudes ranging from 4.6 to 7.1 which can be approximately regarded as point-sources at teleseismic distances while maintaining good signal-to-noise ratio to pass the data quality control process (Text S1). A K-means algorithm (Selim & Ismail, 1984) is used to balance the spatial distribution of the earthquakes. Since the USArray transportable stations are moving, we also balance the temporal distribution of the selected events to fit the station distribution of each stage of USArray (Figure S1a). Generally, 450 - 1,550 stations in the study region for each event are used (Figure S1b). The source parameters are from the global centroid moment tensor (CMT) catalog (Ekström et al., 2012) for most of the earthquakes and SLU regional moment tensor catalog of North America (Herrmann et al., 2011) for the earthquakes inside the contiguous US without global CMT solution. Most of the events have depth within 0 - 50 km, duration between 0 - 7 s and moment magnitude between 5 - 6.6 (Figure S1c-e). The SLU catalog provides a number of Mw 4.5-5 earthquakes within contiguous US which improves the data coverage of eastern US.

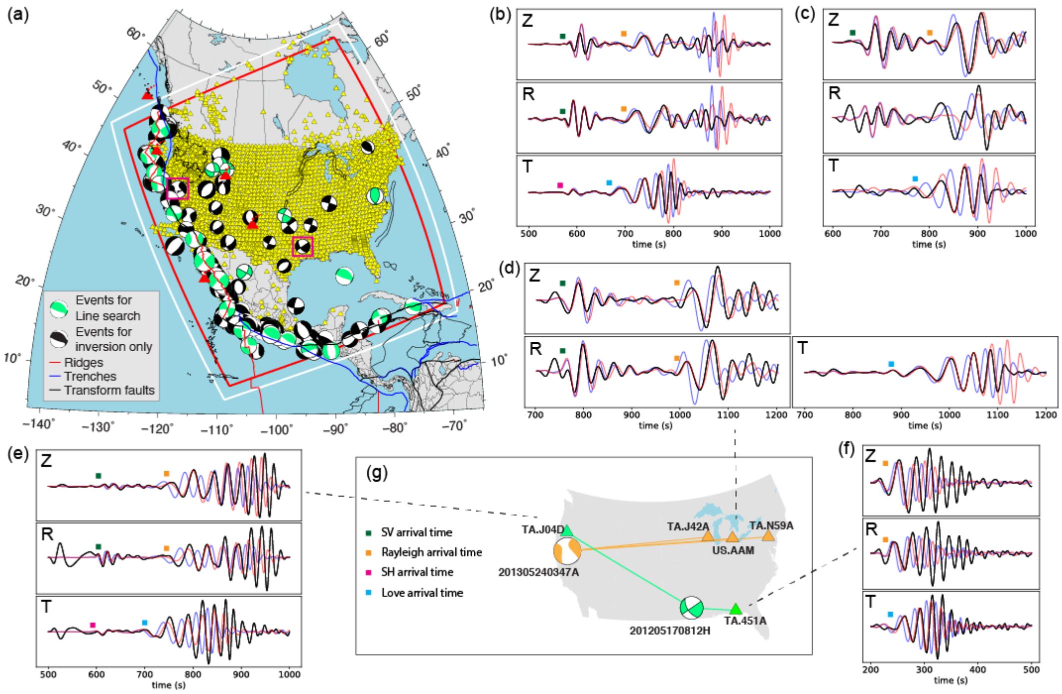

Figure 2. (a) Computational domain, events, and stations (yellow triangles). Events are shown with centroid moment tensor (CMT). Green color are used for line search the optimal model update step. Two of the magenta boxed events are used to demonstrate the waveform fitting of the initial model and final model. White and red boxes are the computational domain and study region excluding a 2-degree margin with absorbing boundary condition. (b-d) waveforms of event 201305240347A recorded at stations TA.J42A, US.AAM and TA.N59A; (e)-(f): waveforms of event 201205170812A recorded at stations TA.J04D and TA.451A; Black curves: observed data; Red curves: synthetic waveforms predicted by model CUSRA2021; Blue curves: synthetic waveforms predicted by the initial model. Colored squares mark the arrival time of seismic phases. (g): Distribution of event-station pairs shown in (b-f).

2.2 Inversion scheme and model parameterization

We apply the full waveform inversion based on adjoint method (Tromp et al., 2005). Wavefield simulation is performed by the SPECFEM3D_GLOBE numerical solver based on the spectral-element method (SEM) (Komatitsch & Tromp, 2002b, 2002a), which combines the accuracy of pseudo-spectral method and the flexibility of finite-element mesh to honor the topography/bathymetry and any laterally varying internal discontinuities of the Earth such as Moho, 410 and 660. It is more accurate in simulating surface waves than finite-difference methods which have stronger numerical dispersion issue (Robertsson, 1996). The effects of Earth's Ocean gravity, ellipticity, 3D complex heterogeneity, attenuation, and anisotropy on seismic wave propagation can also be accurately modeled in the period range of our inversion (15-120 s). Our radially anisotropic wave speed model is parameterized by four parameters: V_c, V_{SV}, V_{SH} and η, which are the bulk compressive wave speed, shear wave speed in vertical and horizontal directions, and the dimensionless parameter representing the wave speeds at oblique propagation directions, respectively. The reason to condense V_{PV} and V_{PH} to one bulk wave speed is that the current data set cannot resolve the P wave anisotropy. The density is scaled to the 0.33 times of the isotropic shear wave speed (Voigt average, $V_s = \sqrt{2/3V_{SV}^2 + 1/3V_{SH}^2}$) perturbations (Anderson, 1987), due to the insensitivity of the seismic phases to density variation. We use anisotropic parameterization from the surface to 670 km discontinuity because in our computational domain, deep mantle data coverage is limited and cannot resolve the radial anisotropy.

2.3 Misfit functions

We only focus on the phase differences between the data and synthetics and apply the frequency-dependent travel time misfit functions in the inversion. Since the large-scale wave speed model for the contiguous US still needs refinement (Zhou et al., 2021, in press), the finite-frequency travel time misfit for long-period body and surface waves is suitable for better constraining the smoothed large-scale wave speed models. The frequency-dependent travel time misfit is measured in three components for P and S waves by cross-correlation of the waveforms and for surface waves by a multi-taper technique (Park et al., 1987; Simons et al., 2000; Y. Zhou et al., 2004) to account for the phase velocity dispersion. An automated window selection code FLEXWIN (Maggi et al., 2009) is used to select the measurement window by comparing the data and synthetics. We combine the measures in six categories: P-SV and Rayleigh waves on vertical (Z) and radial (R) components, and SH and Love waves on tangential (T) components. The assembled misfit function χ^T is:

$$\chi^T = \frac{1}{CN} \sum_c^C \sum_r^N W_c W_r \chi, \tag{1}$$

where χ is the travel time misfit of a single measurement, W_c and W_r are the categorical weighting and geographic weighting factors, respectively. C and N are the total numbers of categories and stations, respectively. The categorical weighting is the inverse of total numbers of measurements in this category, and the geographic weighting balances the station distribution by downweighing the dense array stations, following the algorithm of (Ruan et al., 2019). The combined weighting scheme balances the irregular station distribution and the bias of measurements in each category. We combine intermediate to short period body waves with turning depth from the crust to the upper mantle for $5° - 35°$ epicentral distance in our study region, and long period surface waves that are sensitive to lower crust and uppermost mantle to constrain the crustal and upper mantle wave speed simultaneously. To mitigate cycle skipping, we apply multi-scale inversion strategy by dividing our frequency range into three legs. We start from 20-50 s body waves and 50-120 s surface waves (first leg), and then move to 20-50 s and 30-120 s (second leg), and finally apply 15-50 s and 30-120s (third leg) for body and surface waves, respectively.

2.4 Initial model selection

The nonlinear nature of the full waveform inversion makes it dependent on the initial model. A good initial model is reported to be helpful to prevent the inversion from being trapped into a local minimum (Mulder & Plessix, 2008; Fichtner et al., 2009; Bozdağ et al., 2016; Zhu et al., 2017; Krischer et al., 2018; T. Zhou et al., 2019). The compatibility of crustal and mantle models plays an important role in the radial anisotropy inversion (Bozdağ & Trampert, 2010). Generally, the initial model requires a better data fitting to incorporate more measurement windows which helps the convergence. In order to choose an optimal initial model that is compatible in our SEM mesh and has a good initial data fitting, we compare the data predictability of eight different seismic wave speed models of the contiguous US region using different misfit functions including zero-lag cross-correlation, travel time and waveform least-squares (Zhou et al., in press). The model comparison result suggests an initial model with a smooth global model in the mantle, e.g., S40RTS (Ritsema et al., 2011), combined with a short-period Rayleigh wave constrained crustal model for SV wave speed, e.g., US.2016 (Shen & Ritzwoller, 2016) and Crust1.0 (Laske et al., 2013) for SH wave speed in the crust, has the best predictability and compatibility in our study region. The main advantage for this hybrid initial model is that the short-period Rayleigh wave constrained crust is able to predict intermediate period Rayleigh waves well, which incorporates more measurement windows in the first few iterations of the inversion, while in the mantle, the smoothed version S40RTS does not imprint too much pre-existing details in the inversion, especially for the radial anisotropy. In the SEM mesh, we stretch the spectral elements to honor the Moho of the US.2016 and CRUST1.0 within and outside the contiguous US, respectively. Since the models S40RTS is isotropic, we set the $V_{SV} = V_{SH}$ in the mantle, i.e., there's a zero initial value for radial anisotropy. All the artificial boundaries are smoothed with a Gaussian filter with sigma of 1 degree.

2.5 Model updating

The model is iteratively updated with a conjugate gradient method (Tromp et al., 2005), and the Fréchet kernels are computed by the cross-correlation of forward wavefield and back-propagated adjoint wavefield. The adjoint sources for each event are applying the same categorical and geographical weighting coefficients as the misfit function measurement to balance the kernel. Then kernels for each event are summed up with equal weight and source region masked out with a Gaussian filter with σ of 100 km. Besides, the kernels are pre-conditioned by the approximate Hessian (Luo et al., 2015) and then smoothed with a Gaussian filter that has σ of 100 km in the horizontal plane and σ of 10 km in the vertical direction for the first 7 iterations and for the other iterations, 75 km and 7.5 km, respectively. The step for model updating is determined with a line-search technique using a subset of 24 events (Figure 2a). 5-7 candidate models applying different perturbation steps ranging from 0.005 to 0.05 are tested for searching the best model with minimum data misfit. The optimal updated model is selected as the initial model for the next iteration. Theoretically, the iteration goes on until no significant misfit reduction is observed for each leg. Due to the limitation of the computational resources, we perform 5 iterations for the first and second legs, and 8 iterations for the third leg (Figure 3). The misfit reduction curve starts to be flattened, indicating the convergence of the iteration. The current model manifests significant detailed features of the contiguous US and is named CUSRA2021 (**C**ontiguous **US** **R**adially **A**nisotropic Model of **2021**).

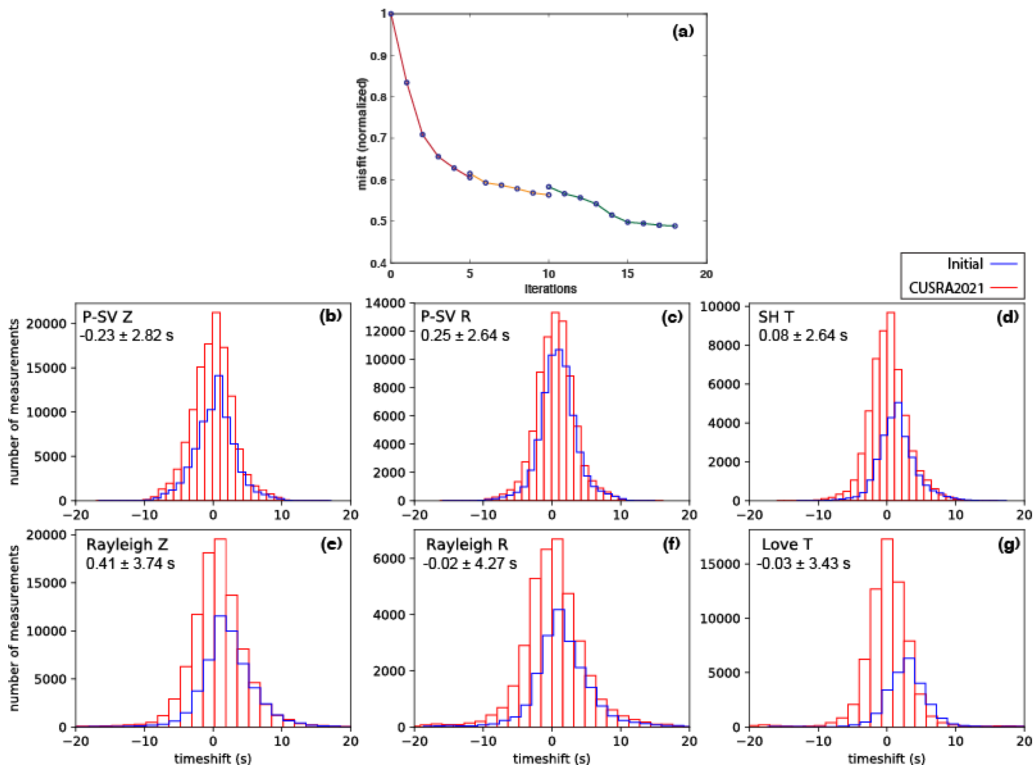

Figure 3. (a) Data misfit with iterations; (b-g) Histogram of travel time shift of available measurement windows in six categories: P-SV on vertical, P-SV on radial, SH on tangential, Rayleigh on vertical, Rayleigh on radial, and Love on tangential. Blue contour marks the initial model (Initial) and red contour marks the current model (CUSRA2021).

3 Model quality assessment

Model quality assessment is significant for evaluating the resolvability and accuracy of the model. We give an estimation of the model resolvability by analyzing the data misfit, data coverage estimated by approximate inverse of Hessian, and point-spread function tests.

3.1 Data misfit

We compare the statistical data misfit with the initial model in Figure 3. The total misfit at the 18th iteration has a 51.6% reduction and the histogram of the travel time measurements in six categories show a significant improvement in terms of the mean travel time misfit (e.g., for SH wave in tangential component from 1.9 s to less than 0.1 s and for Love wave in tangential component from 4.3 s to less than 0.1 s). Besides, the number of the measurement windows increased by 39% in total. Especially, for the Love wave and SH wave measurement windows on tangential components, the number of available measurement windows increased by 77.3%. The model improves the data fitting in tangential components significantly, indicating it has a better constrain on the radial anisotropy than the initial model.

To demonstrate the waveform fitting, we select two earthquake events (Figure 2g), 201305240347A (Mw 5.7 in California) and 201205170812A (Mw 4.8 in Texas), to display the waveform fitting improvement (Figure 2b-f) in a frequency range of 20-80 s. We observe that the waveform fitting of model CUSRA2021 (red curves) has been improved in all three components, especially for the Love waves on T components, compared to the waveform fitting of the initial model (blue curves). The waveform fitting improvement directly demonstrates that the model CUSRA2021 performs well in predicting the waveforms in intermediate period ranges.

3.2 Approximate Hessian

We use approximate Hessian to demonstrate the data coverage (Figure 4a). The approximation of Hessian is computed by cross-correlating forward and adjoint acceleration wavefields (Luo et al., 2015). The data coverage is good across the entire contiguous US in the uppermost mantle, down to the depth of around 200 km. From 200-300 km, the western US and the central US still maintains a good ray coverage, but the eastern coast starts to lose illumination. Near the mantle transition zone at 380 km, only the western US has good data coverage.

3.3 Point-spread function test

We perform point-spread function (PSF) tests to demonstrate the resolution and tradeoff of the model CUSRA2021, following (Fichtner et al., 2010; Chen, Niu, Liu, Tromp, & Zheng, 2015; Zhu et al., 2017). The PSFs are the action of the Hessian on a point-source perturbation of the model, which represents the resolvability of the model configuration that are related to the data coverage. Several high-Vsv Gaussian anomaly with maximum perturbation of 2% and correlation length of 50 km is added to model CUSRA2021 at the depth of 20 and 200 km, respectively. Only Vsv is perturbed in order to analyze the tradeoff between Vsv and Vsh. Figure 4b shows five interested regions with PSF tests in the mantle at 200 km, i.e., Gorda slab, Wyoming block, Colorado Plateau, Illinois and Appalachian Mountain front. In the mantle at 200 km, all the five regions have resolved the PSF. Smearing is observed, possibly along the dominant ray path, in the five regions. Considering the smearing, the resolvability of the model CUSRA2021 is between 100 km and 200 km. There is a little bit tradeoff between Vsv and Vsh, which manifests a more scattered negative Vsh perturbation with about 15% of the amplitude of the Vsv perturbation. The relatively small tradeoff between Vsv and Vsh ensures the resolvability of the radially anisotropic model of the CUSRA2021.

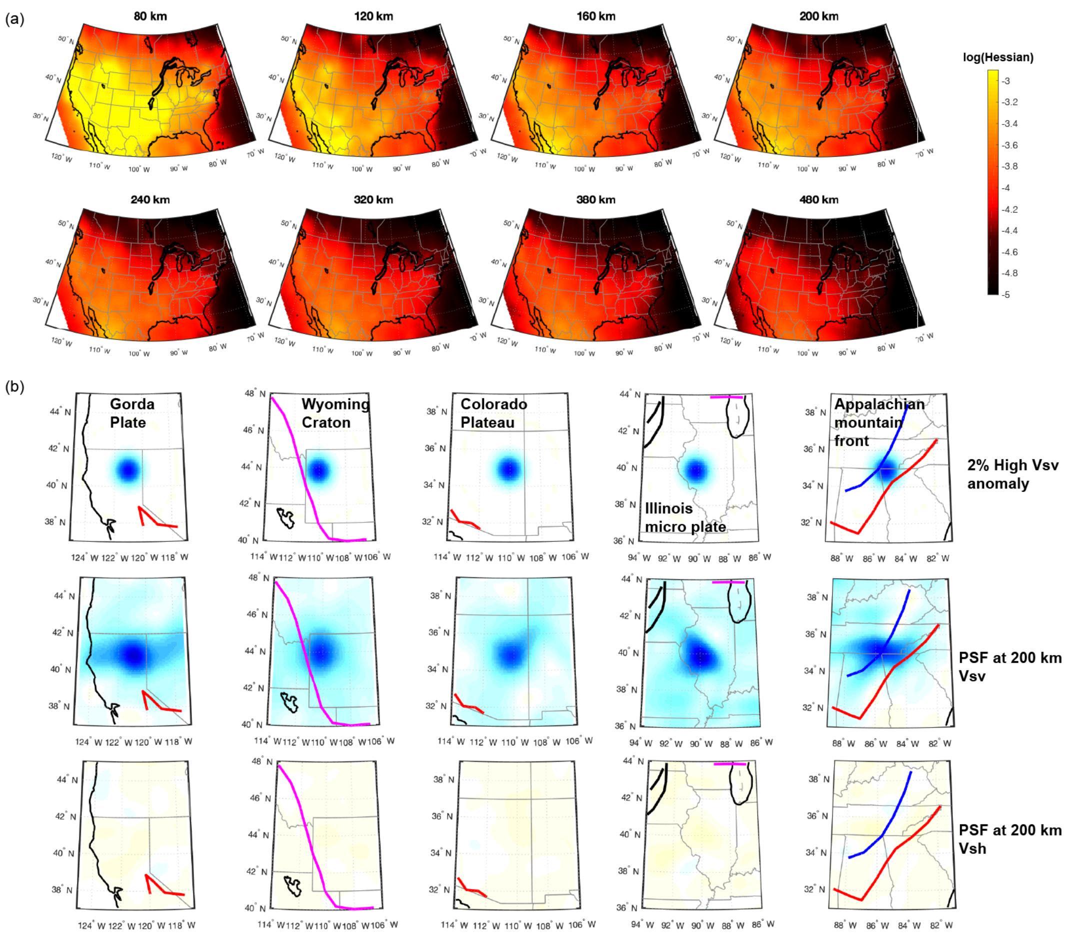

Figure 4. (a) Approximate Hessian in different depths color coded by log scale. Brighter color represents approximately better data coverage and darker color represents lower illumination. From 80 to 380 km. (b) Point-spread function tests in the mantle at the depth of 200 km.

4 Results

We present model CUSRA2021 in the contiguous US region in the crust and mantle using perturbations with respect to the mean velocity of the contiguous US (65-125°W, 25-55°N). Since the highest frequency waveforms incorporated in this model at current stage is 15 s for body waves and 30 s for surface waves, the crustal structure at shallow depths has limited constraints. Besides, our inversion configuration and data set are more sensitive to shear wave speed compared to P wave speed. Therefore, in this section, we focus on shear wave speeds in the mantle. The radial anisotropy for shear wave is presented by the Thomsen parameter $\xi = (V_{SH} - V_{SV})/V_{SV}$ (Thomsen, 1986).

4.1 Shear wave anomalies

To demonstrate CUSRA2021 in the mantle, we plot the isotropic shear wave anomaly (dlnVs) with reference to the mean wave speed of the contiguous US, and the radial anisotropy anomaly (ξ). Figure 5 shows the dlnVs in 80-480 km. The first-order large scale feature is a low-Vs anomaly in the western US and a high-Vs anomaly in the eastern US. The boundary dividing low-Vs and high-Vs anomalies is approximately around the front of Rocky Mountains. In the uppermost mantle (70-120 km), western US has a -5 to -6% low-Vs anomaly and some extremely low-Vs (around -8%) regions in Columbia Plateau, Northern basin and range and Baja California. Colorado Plateau is manifesting a relatively higher-Vs zone (-3%) in the center and a very low-Vs zone (-8%) in the surroundings. In the central and eastern US, on average a 4% high-Vs zone is observed. Approximately larger high-Vs (5 to 6%) regions are observed in two Archean craton cores, Wyoming and Superior. In the upper mantle (160-380 km), the Cascadia subduction zone emerges as a smaller low-Vs anomaly (-1 to -2%) compared to surrounding regions (-3%). Especially the Gorda slab is clearly imaged from 200 to 480 km as a high-Vs (2 to 3%) anomaly and moves towards east as the depth increases. In $160 - 240$ km, large low-Vs anomaly (¿3%) is observed in Baja California and southwestern US and extends to south basin and range near Rio-grenade rift zone. low-Vs anomaly (2%) connecting the Yellowstone hotspot, and the large low-Vs anomaly is also observed. A 2 to 3% high-Vs anomaly is observed in central and east US, correlating with the region of Archean Superior Craton and Proterozoic Cratons. The high-Vs anomaly beneath Proterozoic Cratons around Illinois separates from the high-Vs anomaly beneath Archean Superior Craton. Besides,

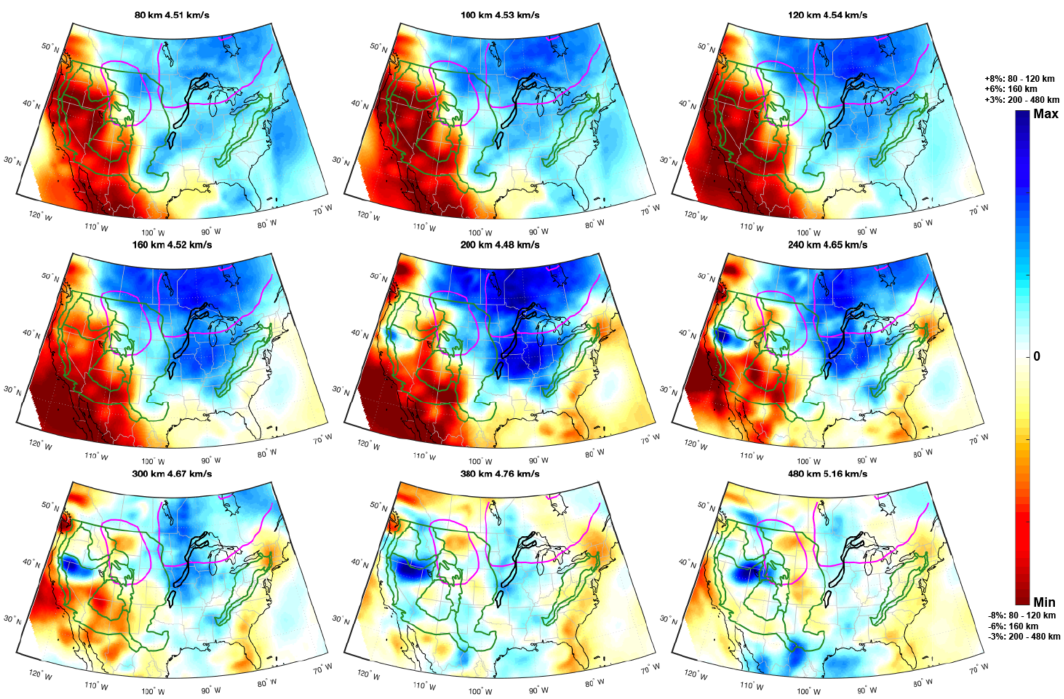

Figure 5. Mantle shear wave speeds model of CUSRA2021. Perturbation of the voigt average of shear wave speed (dlnVs) is plotted with reference to the mean value of the contiguous US region (65-125°W, 25-55°N, marked on each panel). Depths: 80, 100, 120, 160, 200, 240, 300, 380 and 480 km. Contours of geological units are the same as Figure 1

the high-Vs anomaly beneath North America Craton is surrounded by a moderate low-Vs anomaly (-1 to -2%), correlating with the passive continental margin.

4.2 Radial anisotropy

The radial anisotropy anomaly ξ is plotted in Figure 6. In the uppermost mantle (80-120 km), A uniform high ξ (¿5%) is observed. Relatively smaller high-ξ (1-2%) region is observed along the western coast, in the middle of Superior Craton, and along the Mid Continental Rift. The relatively low-ξ region is further enhanced as the depth increases. In 120 to 160 km, such regions become to have low-ξ anomaly. In the upper mantle (160 - 380 km), generally low-ξ (around -1%) is observed. Colorado Plateau and Protozoic cratons around Illinois have relatively large low-ξ (-2%) anomalies at 200 km and extends to 160 and 240 km. For the Wyoming Craton, a high ξ anomaly (2 to 3%) to the west starts to come out at 160 km and continues down to 380 km. At 300 and 380 km, this high-ξ anomaly correlates with the low-Vs anomaly.

4.3 Cross-sections

To examine the cross-sections, we plot four cross-sections along 32°N, 36°N, 40°N and 44°N in Figure 7. We observe the Cascadia and Gorda subduction slab with a high-Vs anomaly in the 44N and 40N cross-sections. The North America Craton region (100W to 75W) is marked with a high-Vs anomaly (2%) down to about 200 km and fastly thinning towards west and slowly thinning towards east. The Wyoming block (110W to 105W at 44N) also has a high-Vs anomaly in the east half but quite shallow to 150 km, while the west half manifests low-Vs anomaly. The Colorado Plateau region (112-105W at 36N) still shows a low-Vs anomaly in the upper mantle, possibly due to the large low-Vs imprint from the initial model. The North America Craton breaks up to three blobs to the south. A uniform high-ξ anomaly is observed across the entire contiguous US. The depth of the high-ξ anomaly is between 120 and 200 km.

4.4 Compare with other FWI models

We compare our model with recent regional full-waveform tomographic models, including US32 (Zhu, Yang, & Li, 2020), Krischer18 (Krischer et al., 2018), and SEMum-NA14 (Yuan et al., 2014). Figure 8 shows the isotropic shear wave velocity comparison in the mantle at two indicative depths for upper mantle and lithosphere boundary, 100 km and 200 km. At 100 km, all the four models correlates well in large-scale shear wave anomalies and resolves detailed structures. Model CUSRA2021, US32 and Krischer18 show indicative low-Vs anomaly (-8%) in the Columbia plateau and southern Rocky Mountains. The Colorado Plateau shows a lower amplitude of low-Vs anomaly (-4%). In the east US, the small scale structures does not correlates well between these models. At 200 km, large-scale structures also correlates very well. Yet model CUSRA2021 and Krischer18 show clear high-Vs anomaly (2%) related to Cascadia subduction zone and Wyoming basin. Model US32 also manifests such feature with relatively lower amplitude of shear wave speed anomaly. Especially, model CUSRA2021 show a clearly separated high-Vs anomaly in midwestern US, centered at Illinois. The similarity between three models CUSRA2021, US32 and Krischer18 is probably because of the incorporation of short-wavelength body and surface waves (¡ 30 s). However, for radial anisotropy, large discrepanicy are observed between these models. At 100 km, models CUSRA2021, SEMum-NA14 and Krischer18 manifests a generally high-ξ radial anisotropy anomaly (2-3%), while model US32 excludes this feature. Regarding the small-scale structure, model CUSRA2021, US32 and Krischer18 generally shows low-ξ radial anisotropy (-1%) along the western coast. In the midwest US, especially around mid-continental rift, all four models generally shows a relatively lower radial anisotropy (-1% - 0%). At 200 km, models CUSRA2021 and US32 shows more small-scale structure yet not correlating each other. Models CUSRA2021 and Krischer18 correlates at the Cascadia subduction zone for high-ξ radial anisotropy (2%) and Colorado Plateau for low-ξ radial anisotropy (-1% to -3%). Model SEMum-NA14 shows a more smoothed feature.

A detailed comparison from 80 km to 430 km is shown in Figure S3. Model CUSRA2021 correlates with other FWI models in large-scale structures from uppermost mantle (70 km) to mantle transition zone (430 km), yet some small-scale structures deviate from other models. For example, the subduction slab of Juan de-Fuca and Gorda plates are enhanced in CUSRA2021 as a +2% high-Vs anomaly from 200 to 430 km. A low-Vs anomaly in northern Wyoming Craton (around central Montana) is also observed in the upper mantle from 250 km to 430 km, which correlates with SEMum-NA14 but are much enhanced. For radial anisotropy (Figure S4), large discrepanicies are still observed from 80 to 430 km and even severe beneath 250 km because of the data coverage of Rayleigh and Love waves are incomplete.

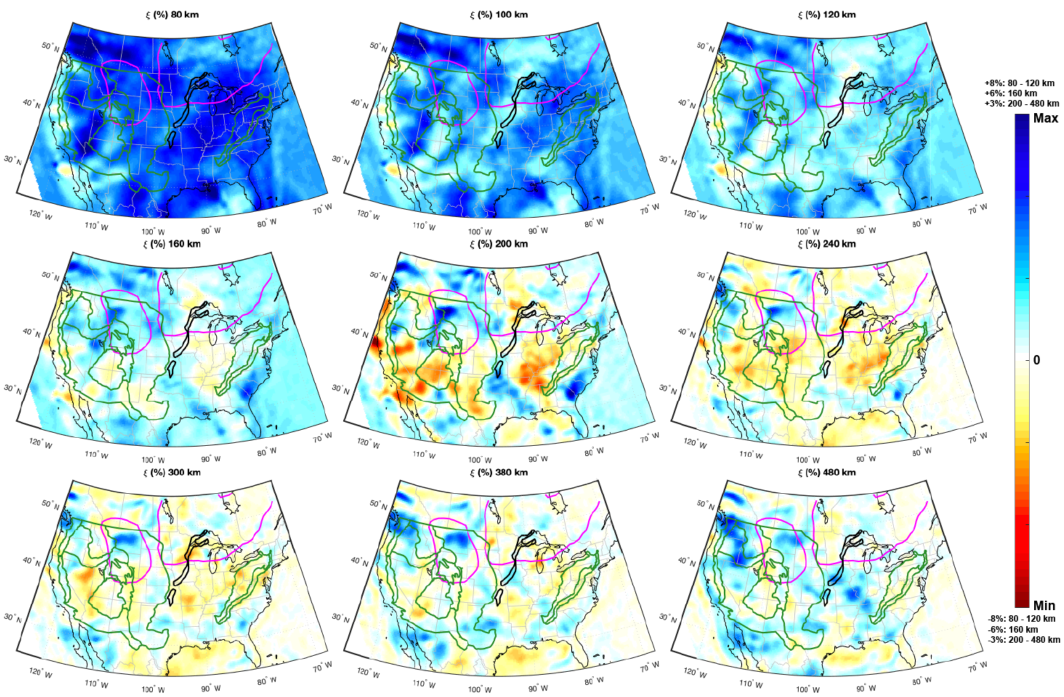

Figure 6. Mantle shear wave radial anisotropy model of CUSRA2021. Depths: 80, 100, 120, 160, 200, 240, 300, 380 and 480 km. Contours of geological units are the same as Figure 1

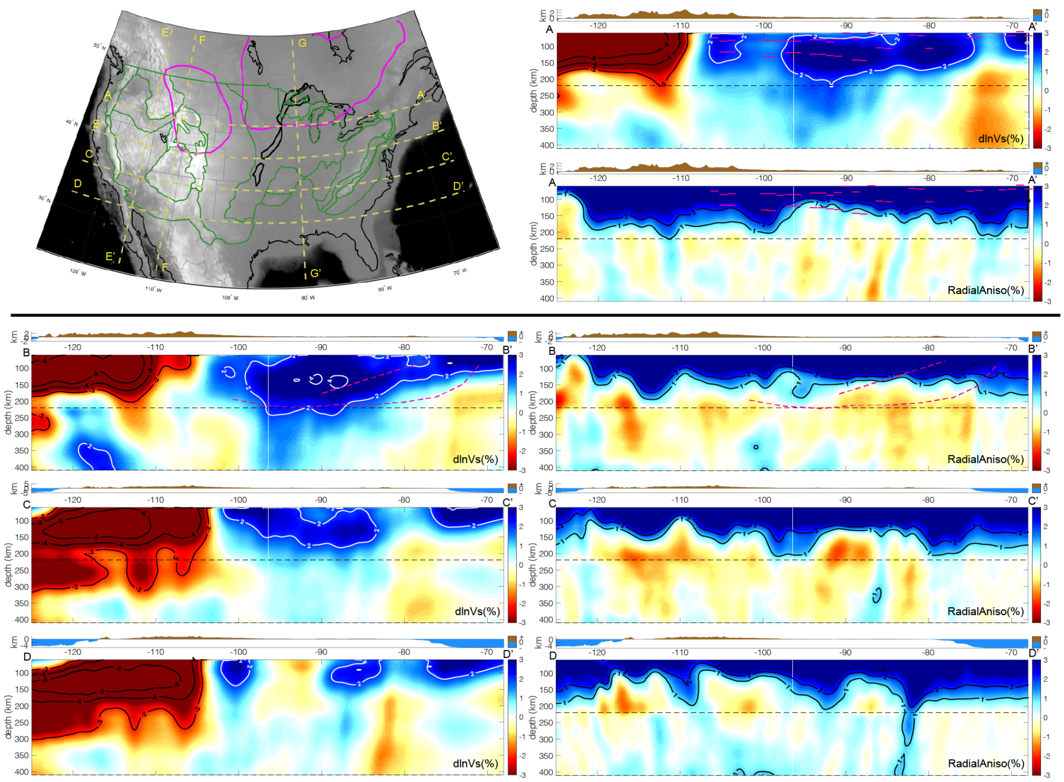

Figure 7. (Black and white panel) Cross sections used in this paper for discussion. (Color panels) Cross section along AA' (44°N), BB' (40°N), CC' (36°N) and DD' (32°N) for the mantle shear wave speeds model of CUSRA2021. Voigt average of shear wave speed perturbation (dlnVs) is plotted in the left column with reference to the mean value of the contiguous US region (65-125°W, 25-55°N). Radial anisotropy anomaly ξ is plotted in the right column. Depth ranges from 60 to 410 km. Magenta bars on profile AA' marks the MLD picks of the SH reflections by Liu et al., 2021. Magenta dashed lines on profile BB' marks the S-to-P reflection constrained LAB depth and "X" interface in the middle of the lithosphere by Kind et al., 2020.

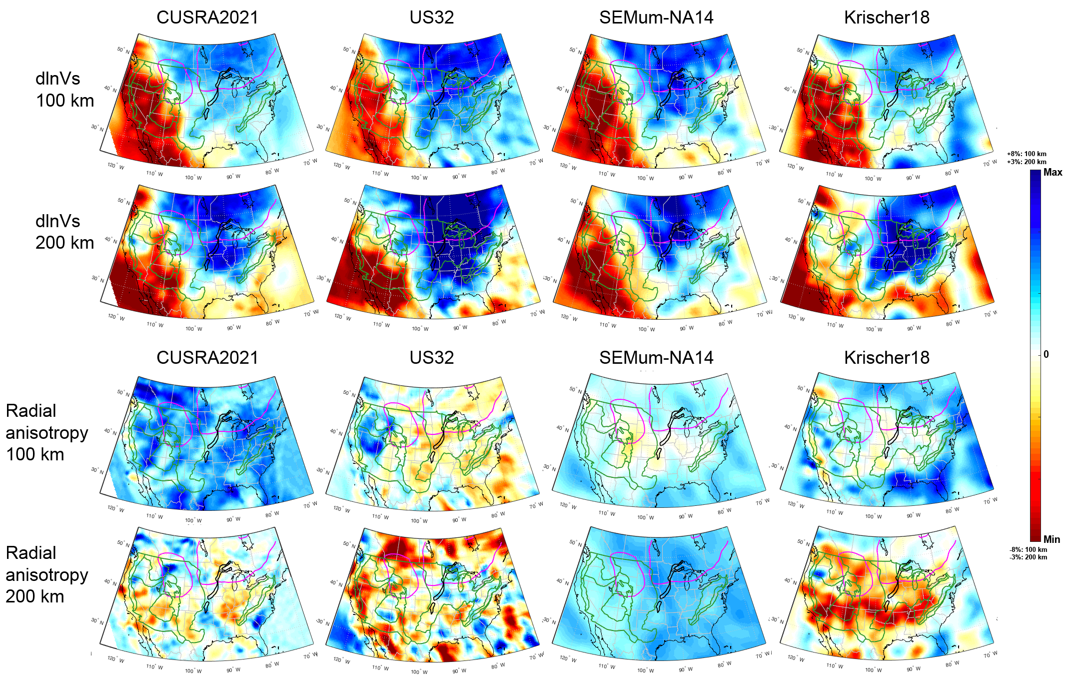

Figure 8. Comparison of CUSRA2021 with other FWI models (US32, SEMum-NA14, and Krischer18) of the US region at the depth of 100 km and 200 km. (Upper 2 rows) shear wave anomaly dlnVs comparison. (Lower 2 rows) Radial anisotropy anomaly ξ comparison.

5 Discussion

Quite a few features including isotropic shear wave anomaly and radial anisotropy anomaly are observed by our model CUSRA2021. The features are indicative for geological units, tectonic events, and deformation processes.

5.1 Low Vs anomaly in western US

We observe several major low shear wave speed anomalies (low-Vs) in the western US. Among which, the most important one is the extremely low-Vs (8%) in the East of Basin and Range Province from 80 to 120 km. The uppermost mantle low-Vs anomaly manifests an elongated north-south trace, ranging from the east end of Columbia Plateau (north) to the south Basin and Range, and turns westward and connects Baja California at the depth of 120 km. Other low-Vs anomalies in the Western US (3-6%) marks the south margin of Columbia Plateau, the boundary of north Basin and Range (NBR), and the boundary of Colorado Plateau. Central NBR and central Colorado Plateau shows relatively lower (1-2%) low-Vs anomaly, which has higher Vs compared to the average velocity of the western US. The elongated low-Vs anomaly can also be observed in vertical cross-sections, i.e., a uniform low-Vs anomaly from 45N to 25N at longitude 115°W (Figure 9). The radial anisotropy map shows a low radial anisotropy anomaly at 30N, indicating that the asthenosphere is getting shallower at Baja California and correlates with the hotspot. The northward trending low-Vs channel in the uppermost mantle is likely to be the partial melting region in the lithosphere which matches the extensive volcanism regions since Neogene (Putirka & Platt, 2012). The origins of the melts are still under debate. One possible hypothesis is that the melting is related to the lithospheric extension due to the arrival of Mendocino Triple Junction (Putirka & Platt, 2012). Here our model provides another hypothesis that the low-Vs channel may represents the transfer of melts from Baja California to Basin and Range province. This low-Vs channel also correlates with model Krischer18 (Krischer et al., 2018) and US-SL-2014 (Schmandt & Lin, 2014).

5.2 Lithosphere thickness of North America Craton

Since our new model incorporates more earthquakes within the contiguous US region, the data coverage in the North America Craton (NAC) region is improved. There-

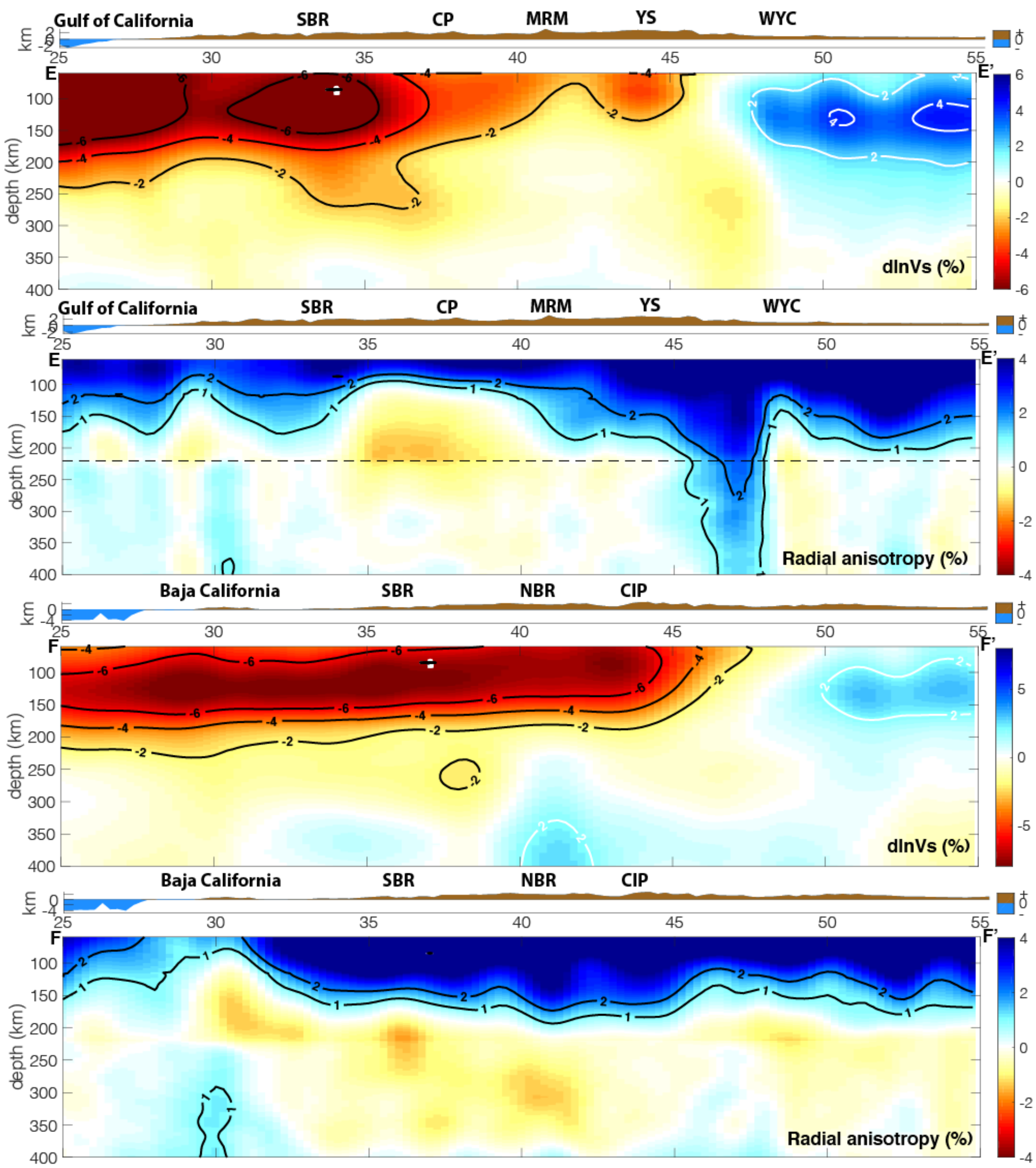

Figure 9. Cross sections along 115°W (EE') and 110°W (FF') for the mantle shear wave speeds and radial anisotropy model of CUSRA2021. The reference shear wave speed is the mean Vs is the contiguous US region (65-125°W, 25-55°N). Depth ranges from 60 to 400 km

fore, model CUSRA2021 can resolve the lithospheric structure of NAC. The main feature of the North America Craton is the high-Vs anomaly from the uppermost mantle to about 200-240 km. Here, we define the lithosphere thickness of the Craton as the boundary of 2% high-Vs anomaly (Lee et al., 2011; Aulbach, 2012; Zheng et al., 2015). The lithosphere thickness is about 200-220 km at the Superior core and 240 km at the Illinois microblock (Stein et al., 2018). The lithosphere thickness correlates with the most recent S-to-P receiver function result (Kind et al., 2020). Another main feature is that the NAC region breaks up into two parts at 200 to 240 km depth. Figure 10 also shows the feature in vertical cross sections along 90W longitude. Superior Craton core has a very strong high-Vs anomaly (5%) and the Proterozoic Craton beneath Illinois (IL microblock, (Stein et al., 2018)) has been separated from the Superior core, indicating a Proterozoic deformation related to the rifting process. From the radial anisotropy cross-section, we observe that there's a continuous boundary of high-ξ region at around 150 km, with some weak variations correlating to the craton cores and gaps.

5.3 High radial anisotropy anomaly across contiguous US

We observe high radial anisotropy anomaly across contiguous US in the uppermost mantle. The high-ξ layer defined by $\xi > 1\%$ extends down to about 120 to 200 km with an average depth of 150 km. Thick high-ξ layer are mainly located beneath the northern Wyoming Craton. The Eastern Coast region also show thick high-ξ region however it is out of the well data coverage regions. The high-ξ layer thinned significantly beneath the Colorado Plateau and Mid-Continental Rift regions. In the North America Craton region, the averaged high-ξ layer depth correlates with the mid-lithosphere discontinuities (Fischer et al., 2010; Yuan & Romanowicz, 2010; L. Liu & Gao, 2018; T. Liu & Shearer, 2021). The radial anisotropy may be an interpretation of the mid-lithosphere discontinuity, which is likely to be related to the modification of lower lithosphere (L. Liu & Gao, 2018), different stages of lithosphere foundering (Yuan & Romanowicz, 2010), and accretion processes of the lithosphere (Bostock, 1998; Courtier et al., 2010).

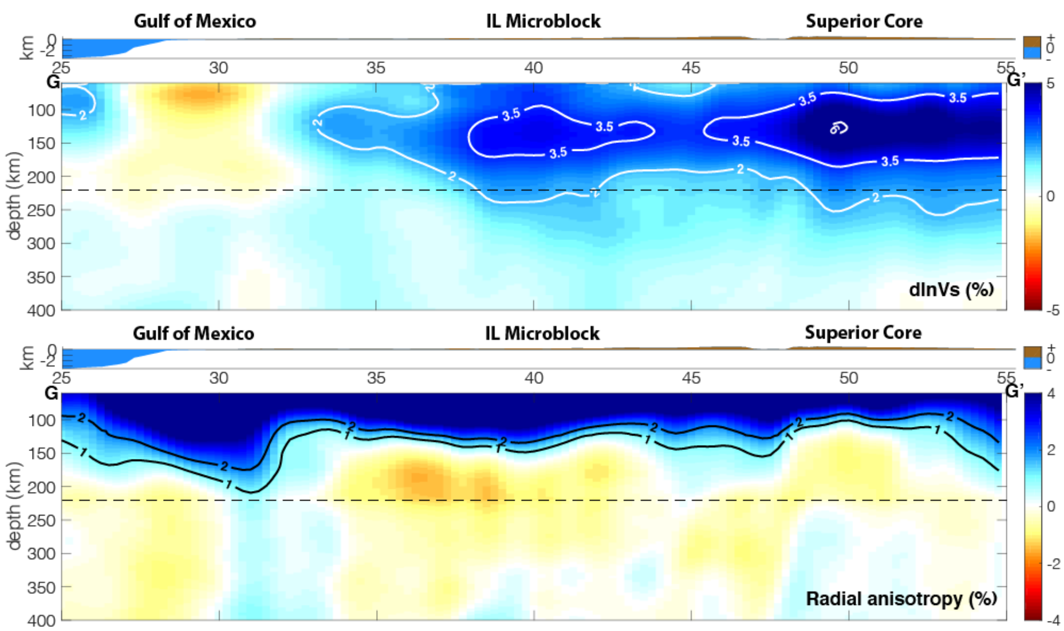

Figure 10. Cross sections along 90°W (GG') for the mantle shear wave speeds and radial anisotropy model of CUSRA2021. The reference shear wave speed is the mean Vs is the contiguous US region (65-125°W, 25-55°N). Depth ranges from 60 to 400 km

6 Conclusion

We present our newly constructed radially anisotropic seismic wave speed model of the contiguous US and surrounding regions: CUSRA2021. This model is constructed based on full-waveform inversion and adjoint methods using three-component waveforms from 160 regional and local earthquakes and all the available stations. The inversion utilizes multiscale technique with three period bands up to 15-50 seconds of body waves and 30-120 seconds for surface waves. The initial model is carefully selected for the optimal initial data availability. Our model correlates well with previous studies and manifests enhanced indicative shear wave speed anomalies and radial anisotropy anomalies. We observe the Craton lithosphere with about 200 km thickness, compatible with thermal studies and receiver function studies. The Gorda subduction slab are enhanced with high-Vs anomalies from the upper mantle to the mantle transition zone. An extremely low-Vs in uppermost mantle of the east Basin and Range province is also observed and correlates well with Neocene volcanisms. The shear wave speed features along with radial anisotropy will provide independent further seismic constrains of some geodynamic features, and help to elucidate highly debating scientific questions including the deformation process of North America Craton, etc.

Acknowledgments

We thank Lion Krischer, Andrew J. Schaeffer, Xyoli Pérez Campos, Robert Herrmann, Qinya Liu, Tianze Liu and Barbara Romanowicz for their constructive discussion and suggestion. We thank the Extreme Science and Engineering Discovery Environment (XSEDE supported by NSF grant ACI-1053575) for providing the high-performance computing resources (XSEDE grant TG-EAR140030 and TG-EES200014) on Stampede2 supercomputer hosted by Texas Advanced Computing Center (TACC). We thank the Institute for Cyber-Enabled Research (ICER) at Michigan State University for providing additional computational resources for data processing. This research was supported by NSF grant 1802247, 1942431 and the startup fund of Min Chen at Michigan State University. We also thank Lingsen Meng and his group members for helpful discussions.

Here we would like to express our special memorial for one of our co-author Dr. Min Chen, who suddenly passed away in July 2021. Min was a brilliant seismologist and her research aimed to better understand plate tectonics and earthquake ruptures using high-resolution seismic images produced by FWI. Min also worked tirelessly to improve di-

versity, equity, and inclusion in the geoscience community. She was always passionate about life and was always ready to help her students, colleagues, and friends all over the world - from Asia, America to Africa. She indeed passed on her kind heart and smile to every friends.

Data and code Acknowledgement

Data and codes related to this paper are all open-source. The open-source spectral-element seismic wave simulation code package SPECFEM3D_GLOBE used for this article are freely available for download via the Computational Infrastructure for Geodynamics (CIG; geodynamics.org). We also used an open-source python package ObsPy (https://github.com/obspy/obspy/) for data downloading and processing. Our broadband seismic data are downloaded from IRIS Data Management Center (IRISDMC, https://ds.iris.edu/ds/nodes/dmc/), Canadian National Data Centre (CNDC, https://www.earthquakescanada.nrcan.gc.ca/stndon/CNDC/index-en.php), and Servicio Sismologico Nacional of Mexico (SSN, http://www.ssn.unam.mx).

Data Availability

The model CUSRA2021 will be uploaded to IRIS Earth Model services and open to public soon. The model is also available by contacting the corresponding author.

References

Anderson, D. L. (1987). A seismic equation of state ii. shear properties and thermodynamics of the lower mantle. *Physics of the earth and planetary interiors*, *45*(4), 307–323.

Aulbach, S. (2012). Craton nucleation and formation of thick lithospheric roots. *Lithos*, *149*, 16–30.

Bostock, M. (1998). Mantle stratigraphy and evolution of the slave province. *Journal of Geophysical Research: Solid Earth*, *103*(B9), 21183–21200.

Bozdağ, E., Peter, D., Lefebvre, M., Komatitsch, D., Tromp, J., Hill, J., . . . Pugmire, D. (2016). Global adjoint tomography: first-generation model. *Geophysical Journal International*, *207*(3), 1739–1766.

Bozdağ, E., & Trampert, J. (2010). Assessment of tomographic mantle models using spectral element seismograms. *Geophysical Journal International*, *180*(3), 1187–1199.

Chen, M., Niu, F., Liu, Q., & Tromp, J. (2015). Mantle-driven uplift of hangai dome: New seismic constraints from adjoint tomography. *Geophysical Research Letters*, *42*(17), 6967–6974.

Chen, M., Niu, F., Liu, Q., Tromp, J., & Zheng, X. (2015). Multiparameter adjoint tomography of the crust and upper mantle beneath east asia: 1. model construction and comparisons. *Journal of Geophysical Research: Solid Earth*, *120*(3), 1762–1786.

Chen, M., & Tromp, J. (2007). Theoretical and numerical investigations of global and regional seismic wave propagation in weakly anisotropic earth models. *Geophysical Journal International*, *168*(3), 1130–1152.

Clouzet, P., Masson, Y., & Romanowicz, B. (2018). Box tomography: first application to the imaging of upper-mantle shear velocity and radial anisotropy structure beneath the north american continent. *Geophysical Journal International*, *213*(3), 1849–1875.

Courtier, A. M., Gaherty, J. B., Revenaugh, J., Bostock, M. G., & Garnero, E. J. (2010). Seismic anisotropy associated with continental lithosphere accretion beneath the canoe array, northwestern canada. *Geology*, *38*(10), 887–890.

Ekström, G., Nettles, M., & Dziewoński, A. (2012). The global cmt project 2004–2010: Centroid-moment tensors for 13,017 earthquakes. *Physics of the Earth and Planetary Interiors*, *200*, 1–9.

Fichtner, A., Kennett, B. L., Igel, H., & Bunge, H.-P. (2009). Full seismic waveform tomography for upper-mantle structure in the australasian region using adjoint methods. *Geophysical Journal International*, *179*(3), 1703–1725.

Fichtner, A., Kennett, B. L., Igel, H., & Bunge, H.-P. (2010). Full waveform tomography for radially anisotropic structure: new insights into present and past states of the australasian upper mantle. *Earth and Planetary Science Letters*, *290*(3-4), 270–280.

Fischer, K. M., Ford, H. A., Abt, D. L., & Rychert, C. A. (2010). The lithosphere-asthenosphere boundary. *Annual Review of Earth and Planetary Sciences*, *38*, 551–575.

Herrmann, R. B., Benz, H., & Ammon, C. J. (2011). Monitoring the earthquake source process in north america. *Bulletin of the Seismological Society of America*, *101*(6), 2609–2625.

Kind, R., Mooney, W. D., & Yuan, X. (2020). New insights into the structural elements of the upper mantle beneath the contiguous united states from s-to-p converted seismic waves. *Geophysical Journal International*, *222*(1), 646–659.

Komatitsch, D., & Tromp, J. (2002a). Spectral-element simulations of global seismic wave propagation—ii. three-dimensional models, oceans, rotation and self-gravitation. *Geophysical Journal International*, *150*(1), 303–318.

Komatitsch, D., & Tromp, J. (2002b). Spectral-element simulations of global seismic wave propagation—i. validation. *Geophysical Journal International*, *149*(2), 390–412.

Krischer, L., Fichtner, A., Boehm, C., & Igel, H. (2018). Automated large-scale full seismic waveform inversion for north america and the north atlantic. *Journal of Geophysical Research: Solid Earth*, *123*(7), 5902–5928.

Laske, G., Masters, G., Ma, Z., & Pasyanos, M. (2013). Update on crust1. 0—a 1-degree global model of earth's crust. In *Geophys. res. abstr* (Vol. 15, p. 2658).

Lee, C.-T. A., Luffi, P., & Chin, E. J. (2011). Building and destroying continental mantle. *Annual Review of Earth and Planetary Sciences*, *39*, 59–90.

Lei, W., Ruan, Y., Bozdağ, E., Peter, D., Lefebvre, M., Komatitsch, D., … Pugmire, D. (2020). Global adjoint tomography—model glad-m25. *Geophysical Journal International*, *223*(1), 1–21.

Lekić, V., & Romanowicz, B. (2011). Inferring upper-mantle structure by full waveform tomography with the spectral element method. *Geophysical Journal International*, *185*(2), 799–831.

Liu, L., & Gao, S. S. (2018). Lithospheric layering beneath the contiguous united states constrained by s-to-p receiver functions. *Earth and Planetary Science Letters*, *495*, 79–86.

Liu, T., & Shearer, P. M. (2021). Complicated lithospheric structure beneath the contiguous us revealed by teleseismic s-reflections. *Journal of Geophysical Research: Solid Earth*, *126*(5), e2020JB021624.

Luo, Y., Modrak, R., & Tromp, J. (2015). Strategies in adjoint tomography. In *Handbook of geomathematics: Second edition* (pp. 1943–2001). Springer Berlin Heidelberg.

Maggi, A., Tape, C., Chen, M., Chao, D., & Tromp, J. (2009). An automated time-window selection algorithm for seismic tomography. *Geophysical Journal Inter-*

national, *178*(1), 257–281.

Mulder, W., & Plessix, R.-E. (2008). Exploring some issues in acoustic full waveform inversion. *Geophysical Prospecting*, *56*(6), 827–841.

Park, J., Lindberg, C. R., & Vernon III, F. L. (1987). Multitaper spectral analysis of high-frequency seismograms. *Journal of Geophysical Research: Solid Earth*, *92*(B12), 12675–12684.

Putirka, K., & Platt, B. (2012). Basin and range volcanism as a passive response to extensional tectonics. *Geosphere*, *8*(6), 1274–1285.

Ritsema, J., Deuss, a. A., Van Heijst, H., & Woodhouse, J. (2011). S40rts: a degree-40 shear-velocity model for the mantle from new rayleigh wave dispersion, teleseismic traveltime and normal-mode splitting function measurements. *Geophysical Journal International*, *184*(3), 1223–1236.

Robertsson, J. O. (1996). A numerical free-surface condition for elastic/viscoelastic finite-difference modeling in the presence of topography. *Geophysics*, *61*(6), 1921–1934.

Ruan, Y., Lei, W., Modrak, R., Örsvuran, R., Bozdağ, E., & Tromp, J. (2019). Balancing unevenly distributed data in seismic tomography: a global adjoint tomography example. *Geophysical Journal International*, *219*(2), 1225–1236.

Schmandt, B., & Lin, F.-C. (2014). P and s wave tomography of the mantle beneath the united states. *Geophysical Research Letters*, *41*(18), 6342–6349.

Selim, S. Z., & Ismail, M. A. (1984). K-means-type algorithms: A generalized convergence theorem and characterization of local optimality. *IEEE Transactions on pattern analysis and machine intelligence*(1), 81–87.

Shen, W., & Ritzwoller, M. H. (2016). Crustal and uppermost mantle structure beneath the united states. *Journal of Geophysical Research: Solid Earth*, *121*(6), 4306–4342.

Simons, F. J., Zuber, M. T., & Korenaga, J. (2000). Isostatic response of the australian lithosphere: Estimation of effective elastic thickness and anisotropy using multitaper spectral analysis. *Journal of Geophysical Research: Solid Earth*, *105*(B8), 19163–19184.

Stein, S., Stein, C. A., Elling, R., Kley, J., Keller, G. R., Wysession, M., … Moucha, R. (2018). Insights from north america's failed midcontinent rift into the evolution of continental rifts and passive continental margins. *Tectono-*

physics, *744*, 403–421.

Tao, K., Grand, S. P., & Niu, F. (2018). Seismic structure of the upper mantle beneath eastern asia from full waveform seismic tomography. *Geochemistry, Geophysics, Geosystems*, *19*(8), 2732–2763.

Tape, C., Liu, Q., Maggi, A., & Tromp, J. (2009). Adjoint tomography of the southern california crust. *Science*, *325*(5943), 988–992.

Tape, C., Liu, Q., Maggi, A., & Tromp, J. (2010). Seismic tomography of the southern california crust based on spectral-element and adjoint methods. *Geophysical Journal International*, *180*(1), 433–462.

Thomsen, L. (1986). Weak elastic anisotropy. *Geophysics*, *51*(10), 1954–1966.

Tromp, J., Tape, C., & Liu, Q. (2005). Seismic tomography, adjoint methods, time reversal and banana-doughnut kernels. *Geophysical Journal International*, *160*(1), 195–216.

Yuan, H., French, S., Cupillard, P., & Romanowicz, B. (2014). Lithospheric expression of geological units in central and eastern north america from full waveform tomography. *Earth and Planetary Science Letters*, *402*, 176–186.

Yuan, H., & Romanowicz, B. (2010). Lithospheric layering in the north american craton. *Nature*, *466*(7310), 1063–1068.

Zheng, J., Lee, C.-T., Lu, J., Zhao, J., Wu, Y., Xia, B., … Liu, Y. (2015). Refertilization-driven destabilization of subcontinental mantle and the importance of initial lithospheric thickness for the fate of continents. *Earth and Planetary Science Letters*, *409*, 225–231.

Zhou, T., Meng, L., Xie, Y., & Han, J. (2019). An adjoint-state full-waveform tsunami source inversion method and its application to the 2014 chile-iquique tsunami event. *Journal of Geophysical Research: Solid Earth*, *124*(7), 6737–6750.

Zhou, Y., Dahlen, F., & Nolet, G. (2004). Three-dimensional sensitivity kernels for surface wave observables. *Geophysical Journal International*, *158*(1), 142–168.

Zhu, H., Bozdağ, E., Duffy, T. S., & Tromp, J. (2013). Seismic attenuation beneath europe and the north atlantic: Implications for water in the mantle. *Earth and Planetary Science Letters*, *381*, 1–11.

Zhu, H., Komatitsch, D., & Tromp, J. (2017). Radial anisotropy of the north american upper mantle based on adjoint tomography with usarray. *Geophysical*

Journal International, *211*(1), 349–377.

Zhu, H., Li, X., Yang, J., Stern, R. J., & Lumley, D. E. (2020). Poloidal-and toroidal-mode mantle flows underneath the cascadia subduction zone. *Geophysical Research Letters*, *47*(14), e2020GL087530.

Zhu, H., Yang, J., & Li, X. (2020). Azimuthal anisotropy of the north american upper mantle based on full waveform inversion. *Journal of Geophysical Research: Solid Earth*, *125*(2), e2019JB018432.

Supplementary material for "CUSRA2021: A Radially Anisotropic Model of the Contiguous US and surrounding regions by full-waveform inversion"

Tong Zhou, Jiaqi Li, Ziyi Xi, Guoliang Li, Min Chen

Introduction

This supplementary material contains 2 texts describing the detailed data quality control process and the comparison between CUSRA2021 and the initial model. This supplementary material has 4 figures showing the statistical property of the data and model comparisons.

Text S1 Data quality control process in detail

We follow a four-step data quality control process. Step 1: Remove mean and linear trend of the raw data, remove the instrument response, convert to displacement, and pre-filter the data to 0.005-0.5 Hz (2 – 200 s). Step 2: Compute the synthetic waveform for each event. Pre-filter the synthetics to 0.005-0.5 Hz (the same as raw data). Then filter the synthetics and the data to the same frequency range of 15-50 s for body waves and 30-120 s for surface waves. We have Step 3: Select windows based on the coherence between observed data and the synthetics using FLEXWIN (Maggi et al., 2009) for body waves and surface waves on vertical, radial, and tangential components, respectively. The cross-correlation coefficient (CC) threshold for accepted windows is 0.65. We then count for window numbers of the 6 categories (body wave and surface wave on Z, R, and T components). Step 4: Events with more than 600 measurement windows in total, and more than 100 measurement windows in each category are counted acceptable and selected.

Text S2 Comparison between model CUSRA2021 and the initial model

Since the initial model has isotropic shear wave speed ($V_{SV} = V_{SH}$), we have uniformly $\xi = 0$ in the mantle for the initial model.

Figure S2 shows the comparison of the shear wave speed anomaly between CUSRA2021 and the initial model. Model CUSRA2021 inherits the large-scale anomalies from the smoothed initial model and manifests a lot more detailed small-scale structures at every depths. Especially, in the upper mantle, strong low-Vs anomaly (-8%) is observed in the Columbia Plateau and South Rocky Mountains. Colorado Plateau has a lower amplitude of low-Vs anomaly (-4%). Cascadia subduction zone is significantly strenghtened by high-Vs anomaly (3%). Proterozoic craton beneath Illinois is strenghtened by high-Vs anomaly (2-3%) and separated from the Archean Superior Craton. Crosssections show clearer evolvation of the NAC from the initial model to CUSRA2021. Cascadia subduction zone is strenghtened at cross-section BB', delamination-like lithosphere can be observed in AA' and BB'. To the south the NAC lithosphere has been separated longitudically on CC' and DD'.

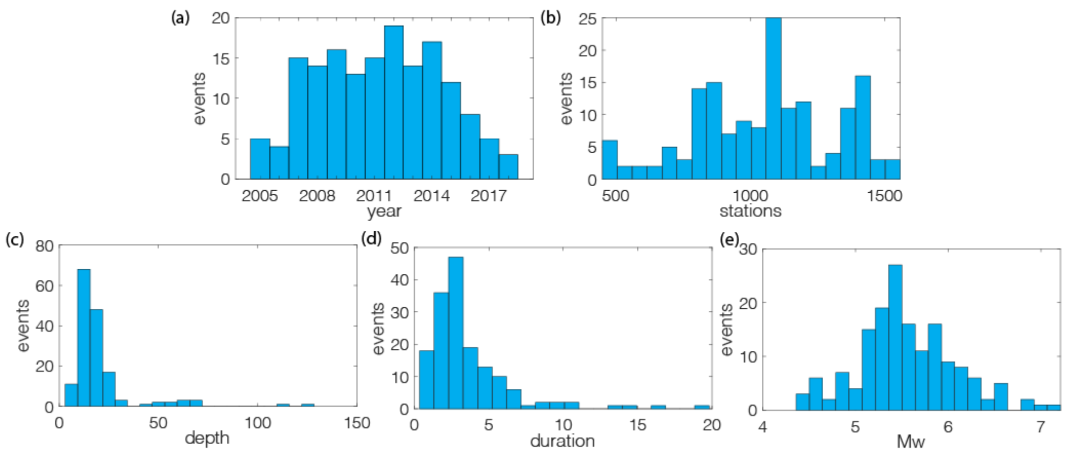

Figure S1. Statistics about earthquake data. (a) event temporal distribution with years. (b) station response distribution for all the events. (c) depth distribution for all the events. (d) duration distribution for all the events. (e) moment magnitude distribution for all the events.

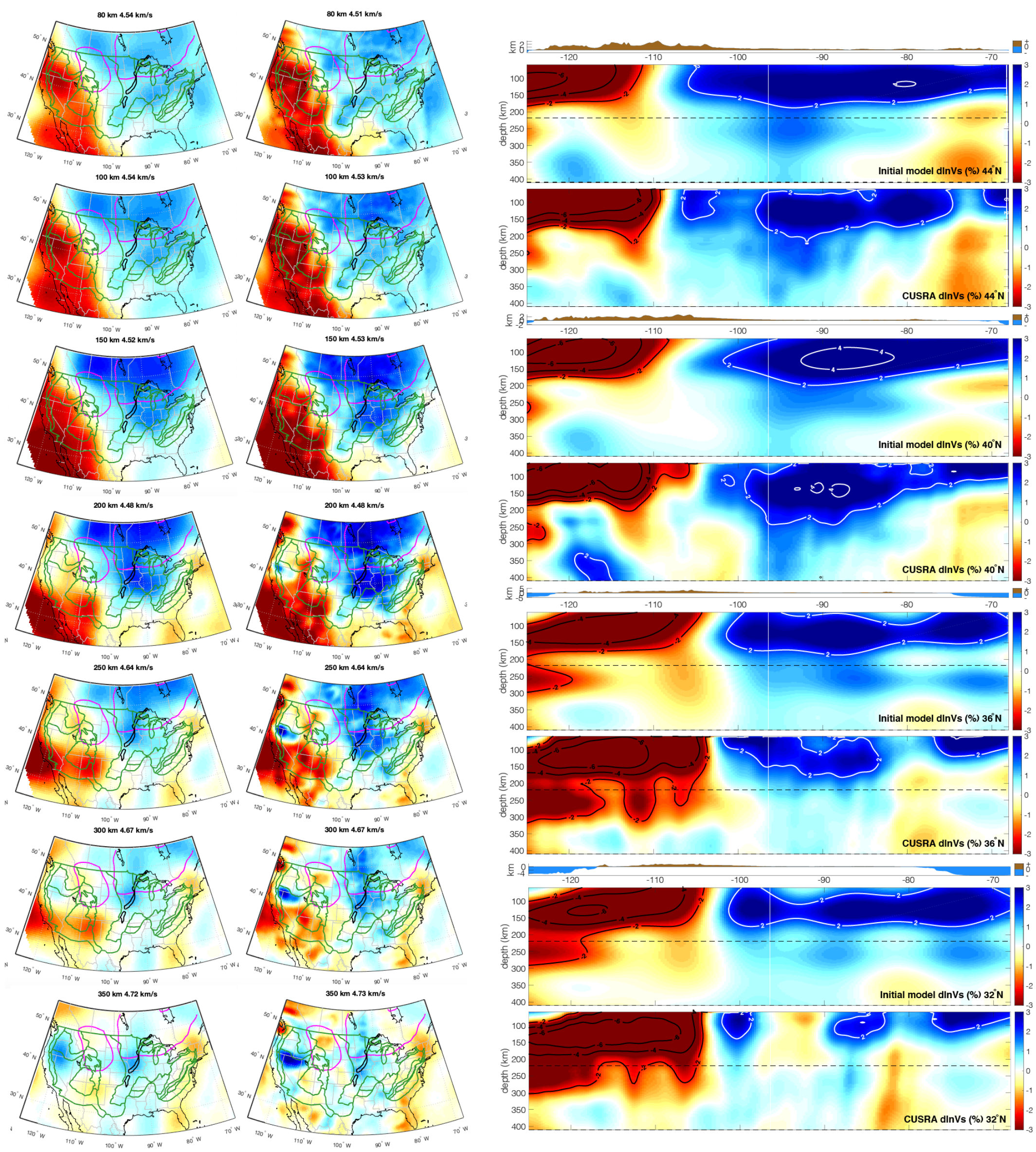

Figure S2. Comparison of the shear wave anomaly of model CUSRA2021 with the initial model. Mapviews: depth range of 80, 100, 150, 200, 250, 300 and 350 km. Left: Initial model; Right: CUSRA2021. Colorscales are the same as Figure 6 in the main text. Cross-sections: along 44N (AA'), 40N (BB'), 36N (CC') and 32N (DD'). The reference shear wave speed is the mean Vs is the contiguous US region (65-125°W, 25-55°N). Depth ranges from 60 to 410 km.

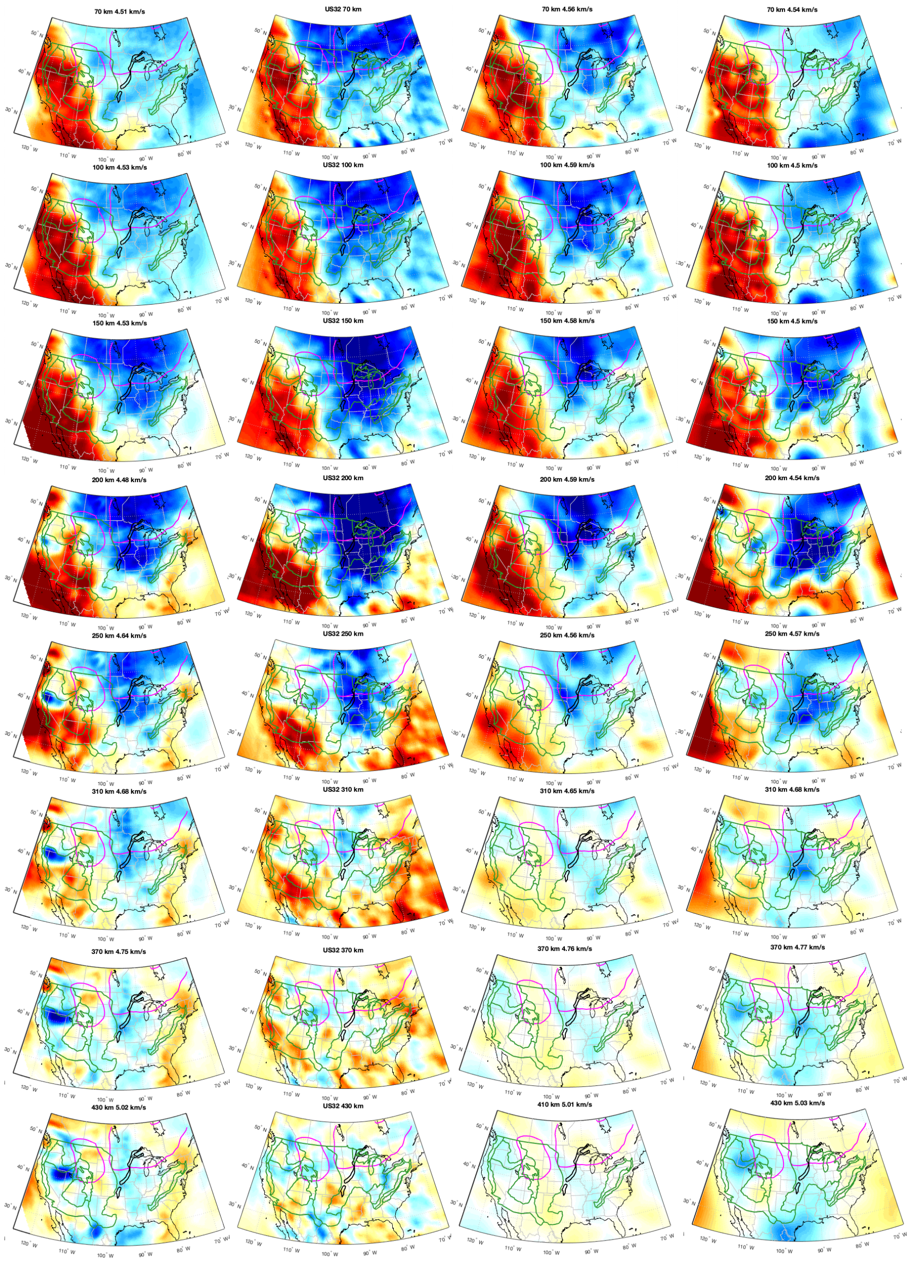

Figure S3. Shear wave model comparison of CUSRA2021 with recent full-waveform tomographic model US32 (Zhu et al., 2020), SEMum-NA14 (Yuan et al., 2014) and Krischer18 (Krischer et al., 2018). Rows: models. Columns: 70, 100, 150, 200, 250, 310, 370, 430 km. Color scales are the same as Figure 8 in the main paper.

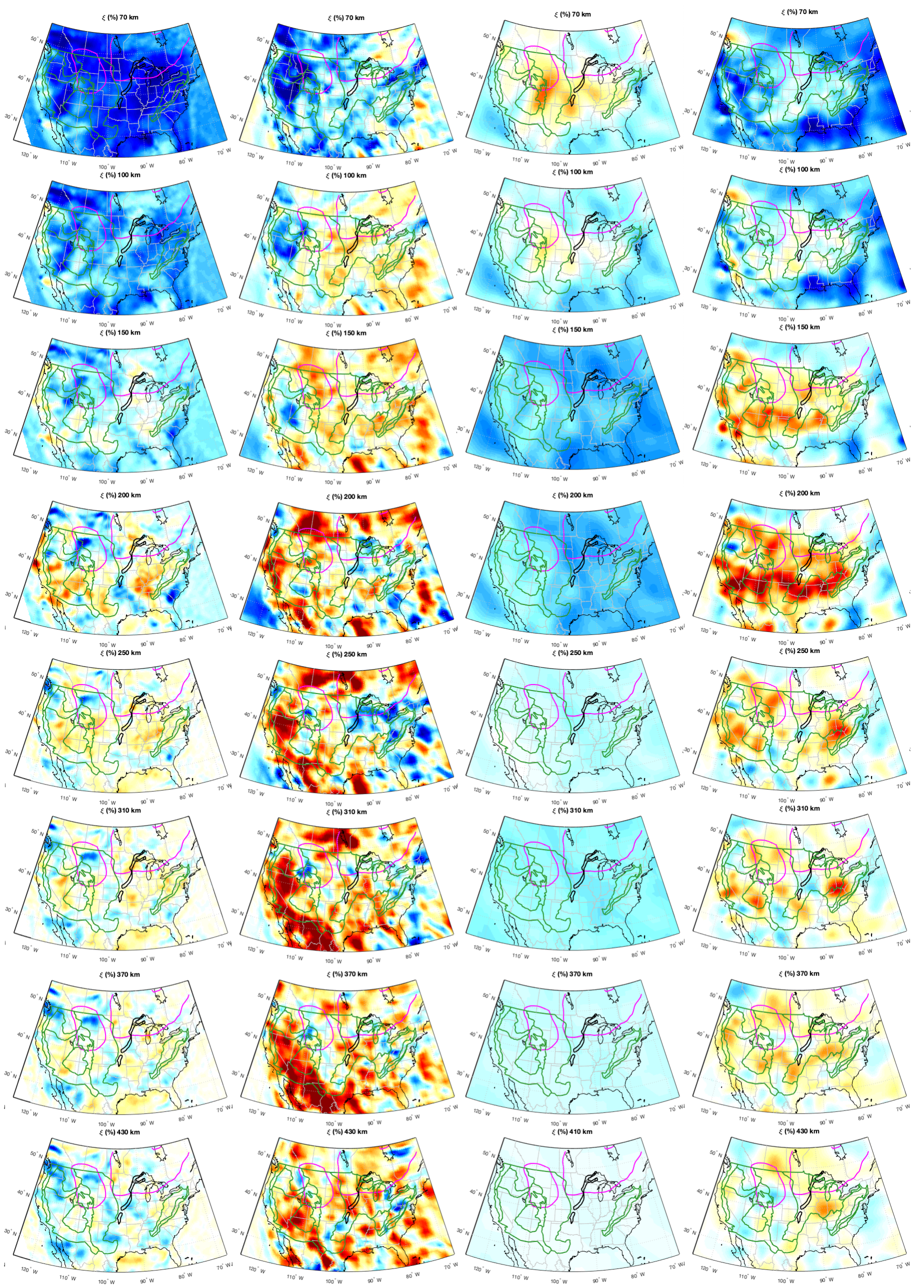

Figure S4. Shear wave radial anisotropy model comparison of CUSRA2021 with recent full-waveform tomographic model US32 (Zhu et al., 2020), SEMum-NA14 (Yuan et al., 2014) and Krischer18 (Krischer et al., 2018). Rows: models. Columns: 70, 100, 150, 200, 250, 310, 370, 430 km. Color scales are the same as Figure 8 in the main paper.